eprints@whiterose.ac.uk
https://eprints.whiterose.ac.uk/

Multiple local symmetries result in a common average polar axis in high strain BiFeO₃ based ceramics

Ge Wang,[a,b] Tengfei Hu,[c, d,*] Wenxuan Zhu,[e] Zhilun Lu,[f] Annette Kleppe,[g] Maria Diaz Lopez,[g] Antonio Feteira,[h] Derek. C. Sinclair,[b] Zhengqian Fu,[c] Houbing Huang,[e,*] Dawei Wang[i,*] and Ian M. Reaney[b]

[a]Department of Materials, University of Manchester, Manchester, S13 9PL, UK
[b]Department of Materials Science and Engineering, University of Sheffield, Sheffield, S1 3JD, UK
[c]State Key Laboratory of High Performance Ceramics and Superfine Microstructure, Shanghai Institute of Ceramics, Shanghai 200050, China
[d]School of Chemistry and Materials Science, Hangzhou Institute for Advanced Study, University of Chinese Academy of Sciences, Hangzhou, 310024, China
[e]Advanced Research Institute of Multidisciplinary Science, and School of Materials Science and Engineering, Beijing Institute of Technology, Beijing, 100081, China
[f]School of Engineering and the Built Environment, Edinburgh Napier University, Edinburgh, EH10 5DT, UK
[g]Diamond Light Source Ltd, Harwell Science and Innovation Campus, Didcot, OX11 0DE, UK
[h]Materials and Engineering Research Institute, Sheffield Hallam University, Sheffield, S1 1WB, UK
[i]Functional Materials and Acousto-Optic Instruments Institute, School of Instrumentation Science and Engineering, Harbin Institute of Technology, Harbin 150080, China

Abstract:

For the first time, the origin of large electrostrain in pseudocubic BiFeO₃-based ceramics is verified with direct structural evidence backed by appropriate simulations. We employ advanced structural and microstructural characterisations of BiFeO₃ based ceramics that exhibit large electrostrain (>0.4%) to reveal the existence of multiple, nanoscale local symmetries, dominantly tetragonal/orthorhombic, which have a common, averaged direction of polarisation over larger, meso/micro- scale regions. Phase-field simulations confirm the existence of local nanoscale symmetries, thereby providing a new vision for designing high-performance lead-free ceramics for high strain actuators.

Piezoelectric materials (e.g. Pb(Zr$_x$Ti$_{1-x}$)O$_3$, PZT) convert mechanical energy into electrical energy and vice versa and play a vital role in a wide range of modern applications, such as sensors, actuators and transducers.[1-3] Due to concerns over the toxicity of lead, recent studies have predominantly focused on the development of lead-free piezoelectrics [4,5] based on compounds such as potassium-sodium niobate (KNN),[6,7] sodium bismuth titanate (NBT) [8] and bismuth ferrite (BF)[9]. However, very few demonstrate competitive performance to replace lead-based incumbents such as PZT.

High electric-field induced strain (electrostrain) in lead-based materials is attributed to several different mechanisms, such as extrinsic contributions (domain switching and structural transformation), intrinsic lattice deformation, multiple phases, polarisation rotations, formation of polar nano-region (PNRs), chemical short-range order and local ferroic order.[10-20] These theories have largely been adapted from lead-based into lead-free materials to explain and/or improve their properties. Phase coexistence has been proposed in NBT- (rhombohedral, R, and tetragonal, T) [8,21] and BF-based (R and pseudo-cubic, PC) [22] compositions with electrostrain >0.3%. Electric field-induced structural transformations also play an important role, particularly for lead-free NBT-based ceramics in which irreversible (nonergodic relaxor) and reversible (ergodic relaxor) transitions occur from PC to long-range R and T symmetries.[23,24] For examples, 0.7% electrostrain was reported by Liu and Tan in NBT-based ceramics due to a phase transition between an ergodic relaxor (nanodomain) to a long range R phase [23], which they observed by in-situ transmission electron microscopy (TEM). 0.38% electrostrain was also obtained in 0.64BiFeO$_3$-0.36BaTiO$_3$ (0.64BF-0.36BT) bulk ceramics due to a transformation from PC to R phase, as evidenced by splitting of the requisite diffraction peaks.[22]

In contrast, a few recent studies on lead-free compositions [25-30] i.e. 0.69BF-0.3BT-0.01Nd(Li$_{0.5}$Nb$_{0.5}$)O$_3$ and 0.6BF-0.4SrTiO$_3$, 0.88NBT-0.05(Sr$_{0.8}$Bi$_{0.1}$)TiO$_{2.95}$-0.06BiZr$_{0.05}$Ti$_{0.95}$O$_3$ and 0.91NBT-0.06BT-0.03KNN ceramics have demonstrated that optimised electrostrain could be realised in a retained PC structure without macroscopic domain switching and long-range structural transformation. Two theories have been proposed to explain this phenomenon: "multiple distorted symmetries" and "bismuth ion displacement" models by Wang et al [25,28] and Kuroiwa et al [26], respectively. However, direct local structure measurements were either absent or limited in each study. In this letter, we have employed a combination of in-$situ$ poling high-energy synchrotron x-ray diffraction (SXRD), x-ray total scattering with pair distribution function analysis (XPDF) and high-angle annular dark-field scanning transmission electron microscopy (HAADF-STEM) to investigate both the macro- and microscopic behaviour of BF-based lead-free ceramics that exhibit large electrostrain (>0.4%). We demonstrate unambiguously the existence of local nanoscale (1-2 nm) multiple symmetries (dominantly T and orthorhombic, O) in an averaged PC lattice for BF-based materials and that large electrostrain can only arise from a common, average direction of polarisation within meso/micro scale regions composed of nanodomains with multiple different symmetries, thereby supporting the model proposed by Wang et al.[25]

A series of lead-free ceramic compositions, (0.7-x) BiFeO$_3$-0.3BaTiO$_3$-xNd(Mg$_{2/3}$Nb$_{1/3}$)O$_3$ (BF-BT-xNMN, x=0.00-0.10), were fabricated using a conventional solid-state method (further experimental details are provided in Supplemental Materials) yielding relative density >94%. Both electric field-polarisation (P-E) and electric field-strain (S-E) were evaluated, resulting in the highest maximum polarisation (P$_{max}$) of 37 μC cm^{-2} and electrostrain of 0.42% for x=0.02 (See Figure S1 of Supplemental Materials) in contrast with only ~0.20% for x=0.00, as reported previously.[25] High-energy in-$situ$ poling SXRD was subsequently carried out on ceramic bar specimens to evaluate the structure under electric field (more experimental details are provided in Supplemental Materials [31,32]) Prior to the application of an electric field (E=0 kV cm^{-1}), full-pattern refinement was performed using TOPAS software and the best-refined result obtained with a single PC structure for x=0.02 (Figure 1a and Figure S2 of

Supplemental Materials) whereas a mixture of *R* (62%) and *PC* (38%) was obtained for x=0.00.[25] Before, during and after application of two full cycles of electric field (up to 100 kV cm^{-1}), all XRD peaks remained symmetric singlets at an orientation vector at β=0˚ (the direction in parallel to external electric field, Figure 1c) and β=90˚ (the direction in perpendicular to external electric field, see Figure S3 of Supplement Materials) and exhibited a horizontal shift as a function of electric field, thereby excluding the possible occurrence of an electric field-induced structural transformation. At β=0˚, peak positions shift to lower 2θ with increasing electric field from 0 to +E$_{max}$, indicating an elongation of the lattice in the direction of the electric field. A large number of reported lead-free materials undergo an electric field-induced irreversible/ reversible structural transformation, evidenced by evolution of their domain morphology (polar nano-regions, PNRs, to ferroelectric lamellae domains) under TEM or peak splitting/merging under SXRD. The absence of changes in peak shape here (Figure 1b) indicates that the origin of electrostrain for these BF-based materials is different to many previously reported.
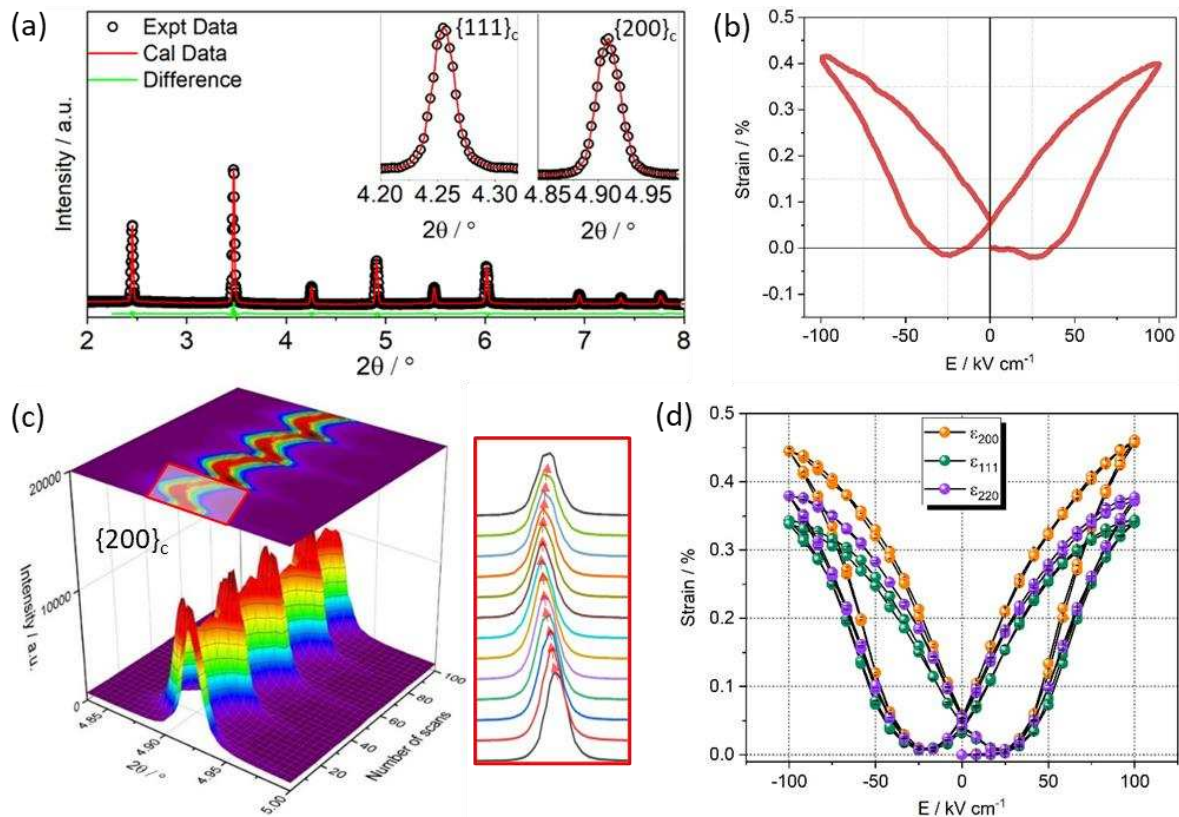

Figure 1. (a) Full-pattern XRD refinement of x=0.02 ceramics using single cubic *Pm$\bar{3}$m* with subfigure of two XRD representative peak profiles of 111 and 200. (b) Experimental measured strain hysteresis curve for x=0.02. (c) 3D and 2D plots of the changes in the XRD 200 peak profile at β = 0˚ as a function of applied electric field. (d) Estimated strains of ε$_{200}$, ε$_{111}$ and ε$_{220}$ calculated from XRD peaks.

Electrostrain is normally estimated by calculation of the strain of individual peaks during *in-situ* poling which can then be used to interpret the experimental origin of macroscopic S-E behaviour, typically accounting for both extrinsic (domain) and intrinsic (lattice) contributions.[33] In this study, the absence of changes in the XRD peak shape precludes this general approach and only the displacement of individual peaks can be assessed. The lattice deformation, obtained from individual peak positions (2θ or d-spacing) as a function of electric field, is shown in Figure 1c. The estimated strains associated with each reflection are 0.34, 0.45 and 0.39% for 111(ε$_{111}$), 200 (ε$_{200}$) and 220 (ε$_{220}$), respectively at 100 kV cm^{-1}. The total estimated strain (S$_{est}$), calculated from XRD peaks, is ~0.41%. This is comparable to the measured macroscopic S$_{max}$~0.42% and dominantly but not exclusively associated with the

displacement of the 200 and equivalent peaks with ε_{200} approximately 30% higher than ε_{111} for x = 0.02. We note that for x=0.00 and 0.05 the difference is <10% (Figure S4 of Supplemental Materials). For long-range ordered ferroelectric ceramics, the estimated lattice strain calculated from the singlet 111 and 200 XRD reflections is used to evaluate the lattice distortion due to domain switching in macroscopic tetragonal and rhombohedral structures, respectively. Here, any occurrence of long-range macroscopic structure is excluded due to the retained average macroscopic *PC* lattice (all singlet and symmetric peaks) throughout in-situ poling. Each of the studied low order reflections therefore, is only affected by local responses (e.g. a local field induced structural transformation or polarisation rotation) and its elastic compliance with the surrounding *PC* matrix. The variation of ε_{111}, ε_{200} and ε_{220} under the applied field suggests there maybe short-range, local distortions corresponding to rhombohedral, tetragonal and orthorhombic structures within an average macroscopic *PC* lattice. Thus it is critical to reveal the origin of these local distortions, as an optimisation strategy to enhance electrostrain in lead-free BF-based materials.

To further study local distortions, HAADF-STEM imaging of the electrostrain optimised composition (x=0.02) was performed on a Cs-corrected Hitachi HF5000 microscope. We note that no large wedge/tweed domains were observed in preliminary TEM studies and local regions were assigned an uneven distribution of *PC* and *R* phases, based on superstructure reflections in diffraction patterns (See Figure S5 of Supplemental Materials). Local distortions corresponding to different symmetries were determined by B-site cation sites relative to the centre of 4 A-site cations, Figure 2a. The atomic column positions (light red and green arrows) at picometer-precision fitting were performed using MATLAB software. [34,35] The polarisation vectors are shown in pink with *T/O* along <001> and yellow areas with *R/O* along <110> directions, respectively. The distorted clusters deviate from the average *PC* lattice with a correlation length of ~1-2 nm. Local lattice anisotropic distortions, obtained by calculating lattice parameter between [001] and [100] directions (Figure 2b) based on the HADDF-STEM image, were 0.98 to 1.07, varying as a function of distance across the HADDF-STEM image due to local structural and strain heterogeneity. XPDF box-car analysis [36] provides a further opportunity to examine the local structure (2-52 Å) of x=0.02 (Figure 2c and 2d) with experimental/analysis details provided in Supplemental Materials. Figure 2c shows the XPDF data (2-22 Å) for x = 0.02, 0.05 and 0.10. Overall, these three G(r) profiles are similar with only slight differences in peak intensity and shape. Combinations of structural models, including *C*, *T*, *R* and O, were used to fit the apparent local structure (<22 Å) (See Figure S6 of Supplemental Materials). A single *Pm$\bar{3}$m* structure gives the poorest fit (R_w~16%) with the best refinement (R_w ~10 %) for x=0.02 (largest electrostrain) obtained with a mixture of *T (31%), O* (34%) and *R* (35%) phases. For x = 0.05, the best-refined structure (R_w~11%) was obtained with the *R* phase being dominant. For x = 0.02, the *T* distortion obtained from the box-car analysis (Figure 2d) has a c/a=1.062 at a r ~12 Å but decreases to c/a=1.005 as r increases. The microscopic and XPDF results therefore, confirm the existence of multi-symmetry (dominantly *T* and O phases) at the nanoscale providing new insight to tailor the electromechanical responses by optimising local structure.
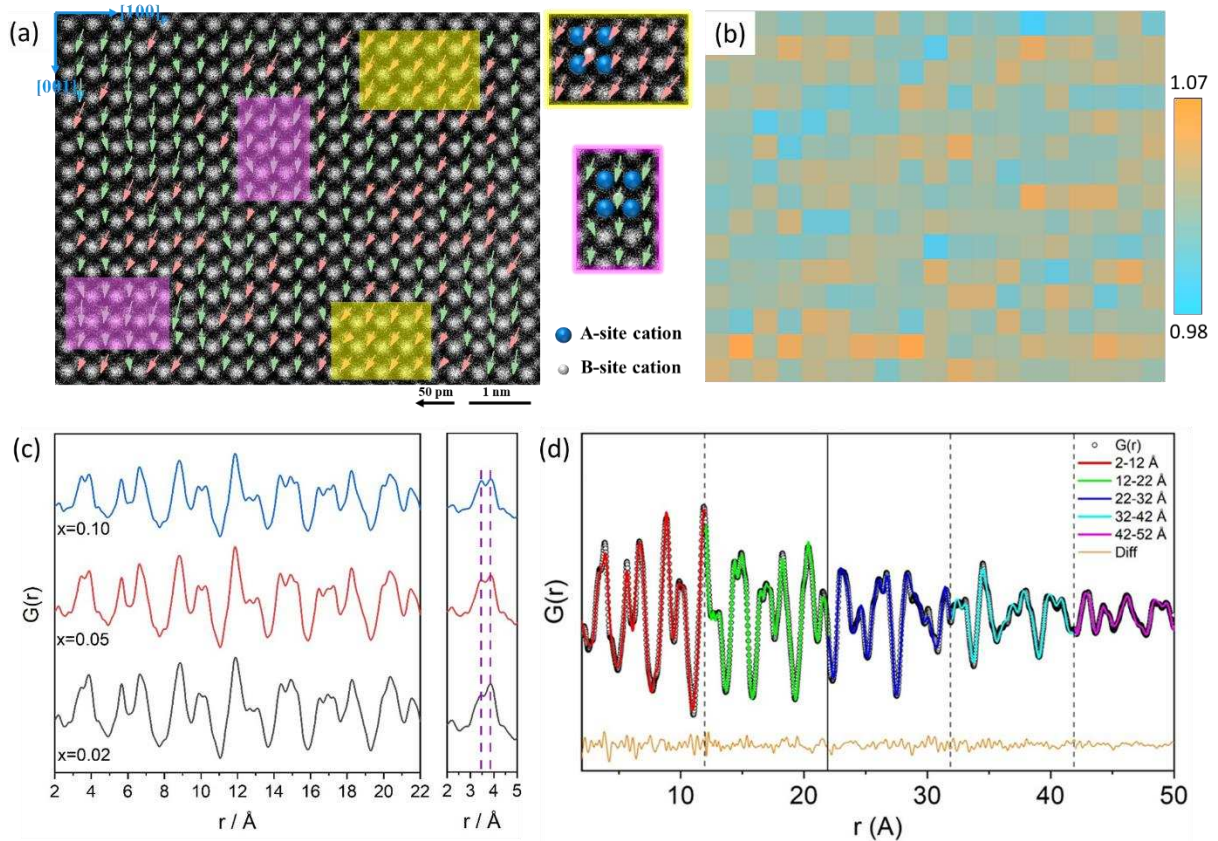
Figure 2. (a) The [010]$_p$-oriented HAADF STEM images for x=0.02. Yellow and pink areas are distorted symmetries, with magnified images with different polarisation directions. The blue and grey spheres represent A and B-site cations, respectively. (b) Local lattice anisotropic distortion mapping cross HAADF-STEM image. (c) XPDF G(r) plots (r=2-22 Å) for compositions with x=0.02, 0.05 and 0.10 with expanded peak profiles of r=2-5 Å. (d) "Box-car" fitting for x=0.02 in a r range of 2-50 Å.

The direct HAADF STEM observations and local structure refinements revealing perturbations in symmetry away from macroscopic *PC* are reported in BF based ceramics for the first time. They confirm a model unlike those previously used to explain piezoelectric or electrostrictive properties, which typically classify materials as either long-range ferroelectrics or short-range relaxor-ferroelectrics; the latter composed of PNRs of the same symmetry. Previous studies under external electric field have proposed that short correlation length in relaxor-ferroelectrics tends to propagate to a medium or long-range ferroelectric state (either irreversible and reversible). For example, La doped BF-PbTiO₃ ceramics have recently been reported with large electrostrain over 1%,[37] mainly due to i) an irreversible structural transformation from *PC* to *T* structure, ii) strong ferroelectric and ferroelastic domain switching, and iii) lattice deformation. Here, the local structure retains short-range correlations regardless of poling/applied field but nonetheless remains electromechanically active. Effectively, the material has a macroscopic direction of polarisation, strain averaged across multiple symmetry local nano-regions, resulting from the occupation of ions of different radius, valence and polarisability on the A and B-sites. In particular, the Ba^{2+} and Bi^{3+} have very different ionic radii and polarisabilities.[38]

To further establish the validity of this model, phase-field simulations were performed with more details of the method provided in Supplemental Materials.[39-42] A two-phase model was employed initially for the BF-BT matrix due to the lack of potential functions.[18] Although the phase ratio is slightly different from the experimental observation, the simulations nonetheless provide theoretical

guidance to understand the experimental results. We note that substitution of NMN in the BF-BT structure reduces the Curie maximum indicating solid solubility, with the electrostrain and charge locally differing due to mismatch in ionic radii and valence, as suggested above. The phase-field simulations of P-E and S-E curves, as well as domain structures of BF-BT (x=0.00) and BF-BT-0.02NMN (x=0.02) are shown in Figure 3. The P-E curve for x=0.02 is slightly slimmer with lower P_{max} than x=0.00 (Figure 3a), yet the electrostrain is significantly higher (Figure 3b). Although the absolute values from P-E and S-E loops do not precisely match the experimental values, electrostrain is clearly enhanced by substituting NMN (x=0.02) into the BF-BT matrix. The comparison of the domain structure between x=0.00 and x=0.02 is shown in Figure 3c and 3d, respectively. Undoped BF-BT (x=0.00) exhibits a dominant long-range R phase (55.9%) whereas the BF-BT-0.02NMN (x=0.02) displays local distortion ascribed to multiple symmetries of mainly $T+O$ (69.8%) phases with minor R (30.2%), concomitant with a reduced domain size (≥1 nm). The phase-field simulations support the experimental observations therefore, of enhanced electrostrain for x=0.02, attributed to a decrease in the domain size and volume fraction of T and O symmetries, supporting SXRD and HAADF data.
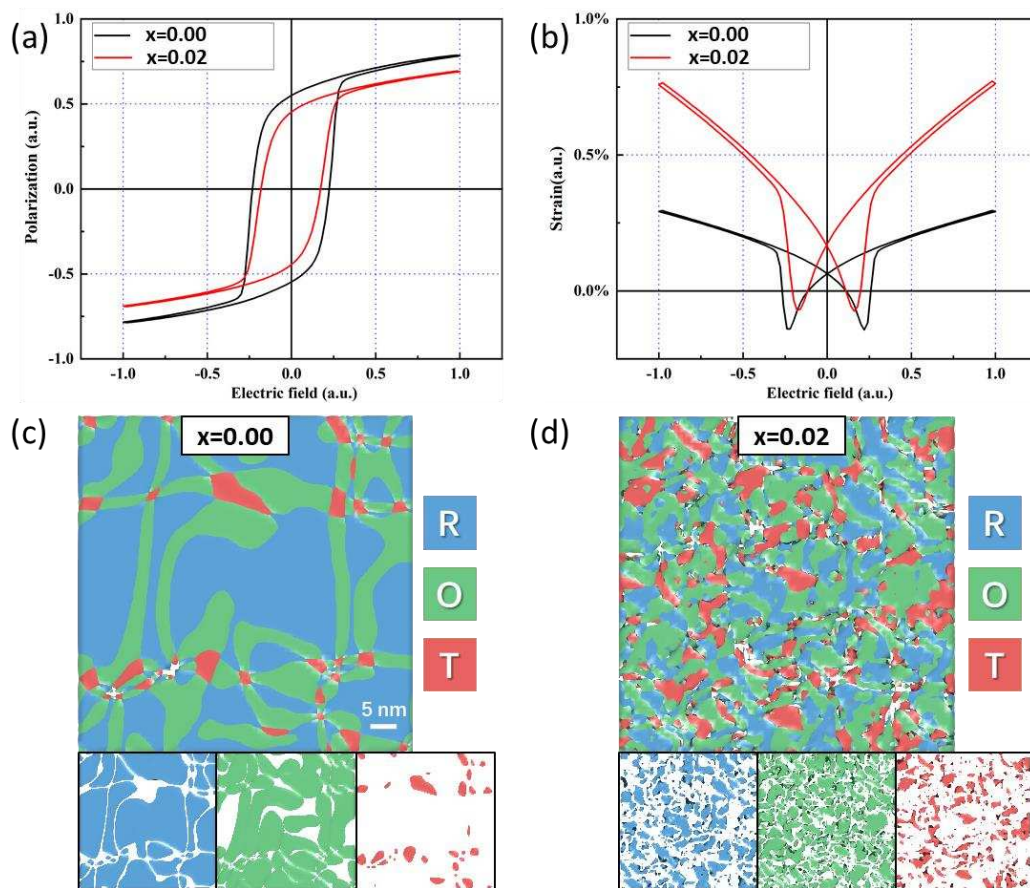

Figure 3. The phase-field method simulated (a) P-E and (b) S-E loops for x=0.00 and x=0.02. The simulated domain structures of (c) x=0.00 and (d) x=0.02. In the domain structure, three colours represent rhombohedral (blue, sub-figure), orthorhombic (green, sub-figure) and tetragonal (red, sub-figure) domains.

In summary, a lead-free BF-based composition displays large electrostrain (>0.4%) but remains macroscopically PC, prior, during and after application of an electric field. The estimated individual peak strain exhibits strong anisotropy, dominantly T/O (65%), 30% greater than R. Direct observation of local distortions using HADDF-STEM and XPDF local structure refinements identify multiple local symmetries (dominant $T+O$ phases) within an averaged PC lattice. Under an electric field, multiple

symmetries support a common average direction of polarisation and strain without transforming to a conventional long-range ordered ferroelectric. Phase-field simulations verify the experimental observations that NMN enhances strain, reduces domain size and promotes the presence *T* and *O* distorted symmetries. The work therefore presents a new paradigm for the optimisation of electrostrain through control of local structure.

Reference

[1]   B. Jaffe, W. R. Cook, and H. L. Jaffe, *Piezoelectric ceramics,* (R.A.N. Publishers, Marietta, Ohio, 1990).

[2]   S.-E. Park and T. R. Shrout, Ultrahigh strain and piezoelectric behavior in relaxor based ferroelectric single crystals, Journal of Applied Physics **82**, 1804 (1997).

[3]   M. Ahart *et al.*, Origin of morphotropic phase boundaries in ferroelectrics, Nature **451**, 545 (2008).

[4]   J. Rödel, W. Jo, K. T. P. Seifert, E.-M. Anton, T. Granzow, and D. Damjanovic, Perspective on the Development of Lead-free Piezoceramics, Journal of the American Ceramic Society **92**, 1153 (2009).

[5]   E. Aksel and J. L. Jones, Advances in Lead-Free Piezoelectric Materials for Sensors and Actuators, Sensors **10**, 1935 (2010).

[6]   Y. Saito, H. Takao, T. Tani, T. Nonoyama, K. Takatori, T. Homma, T. Nagaya, and M. Nakamura, Lead-free piezoceramics, Nature **432**, 84 (2004).

[7]   X. Lv, J. Zhu, D. Xiao, X.-x. Zhang, and J. Wu, Emerging new phase boundary in potassium sodium-niobate based ceramics, Chemical Society Reviews **49**, 671 (2020).

[8]   W. Jo, R. Dittmer, M. Acosta, J. Zang, C. Groh, E. Sapper, K. Wang, and J. Rödel, Giant electric-field-induced strains in lead-free ceramics for actuator applications – status and perspective, Journal of Electroceramics **29**, 71 (2012).

[9]   M. H. Lee, D. J. Kim, J. S. Park, S. W. Kim, T. K. Song, M.-H. Kim, W.-J. Kim, D. Do, and I.-K. Jeong, High-Performance Lead-Free Piezoceramics with High Curie Temperatures, Advanced Materials **27**, 6976 (2015).

[10]   L. Fan, J. Chen, Y. Ren, Z. Pan, L. Zhang, and X. Xing, Unique Piezoelectric Properties of the Monoclinic Phase in Pb(Zr, Ti)O_3 Ceramics: Large Lattice Strain and Negligible Domain Switching, Physical Review Letters **116**, 027601 (2016).

[11]   H. Liu, J. Chen, L. Fan, Y. Ren, Z. Pan, K. V. Lalitha, J. Rödel, and X. Xing, Critical Role of Monoclinic Polarization Rotation in High-Performance Perovskite Piezoelectric Materials, Physical Review Letters **119**, 017601 (2017).

[12]   H. Liu, J. Chen, H. Huang, L. Fan, Y. Ren, Z. Pan, J. Deng, L.-Q. Chen, and X. Xing, Role of Reversible Phase Transformation for Strong Piezoelectric Performance at the Morphotropic Phase Boundary, Physical Review Letters **120**, 055501 (2018).

[13]   B. Noheda, D. E. Cox, G. Shirane, S. E. Park, L. E. Cross, and Z. Zhong, Polarization Rotation via a Monoclinic Phase in the Piezoelectric 92%PbZn$_{1/3}$Nb$_{2/3}$O$_3$-8%PbTiO$_3$, Physical Review Letters **86**, 3891 (2001).

[14]   Y. Li, Y. Chen, Z. Zhang, A. Kleppe, and D. A. Hall, In-situ XRD study of actuation mechanisms in BiFeO$_3$-K$_{0.5}$Bi$_{0.5}$TiO$_3$-PbTiO$_3$ ceramics, Acta Materialia **168**, 411 (2019).

[15]   M. Eremenko, V. Krayzman, A. Bosak, H. Y. Playford, K. W. Chapman, J. C. Woicik, B. Ravel, and I. Levin, Local atomic order and hierarchical polar nanoregions in a classical relaxor ferroelectric, Nature Communications **10**, 2728 (2019).

[16]   M. J. Krogstad *et al.*, The relation of local order to material properties in relaxor ferroelectrics, Nature Materials **17**, 718 (2018).

[17]   A. Kumar, J. N. Baker, P. C. Bowes, M. J. Cabral, S. Zhang, E. C. Dickey, D. L. Irving, and J. M. LeBeau, Atomic-resolution electron microscopy of nanoscale local structure in lead-based relaxor ferroelectrics, Nature Materials **20**, 62 (2021).

[18]   L. Yang *et al.*, Simultaneously achieving giant piezoelectricity and record coercive field enhancement in relaxor-based ferroelectric crystals, Nature Communications **13**, 2444 (2022).

[19]   F. Li *et al.*, The origin of ultrahigh piezoelectricity in relaxor-ferroelectric solid solution crystals, Nature Communications **7**, 13807 (2016).

[20]   F. Li *et al.*, Ultrahigh piezoelectricity in ferroelectric ceramics by design, Nature Materials **17**, 349 (2018).

[21]   J. E. Daniels, W. Jo, J. Rödel, V. Honkimäki, and J. L. Jones, Electric-field-induced phase-change behavior in $(Bi_{0.5}Na_{0.5})TiO_3$–$BaTiO_3$–$(K_{0.5}Na_{0.5})NbO_3$: A combinatorial investigation, Acta Materialia **58**, 2103 (2010).

[22]   J. Chen, J. E. Daniels, J. Jian, Z. Cheng, J. Cheng, J. Wang, Q. Gu, and S. Zhang, Origin of large electric-field-induced strain in pseudo-cubic $BiFeO_3$–$BaTiO_3$ ceramics, Acta Materialia **197**, 1 (2020).

[23]   X. Liu and X. Tan, Giant Strains in Non-Textured $(Bi_{1/2}Na_{1/2})TiO_3$-Based Lead-Free Ceramics, Advanced Materials **28**, 574 (2016).

[24]   J. E. Daniels, W. Jo, J. Rödel, and J. L. Jones, Electric-field-induced phase transformation at a lead-free morphotropic phase boundary: Case study in a $93\%(Bi_{0.5}Na_{0.5})TiO_3$–$7\%BaTiO_3$ piezoelectric ceramic, Applied Physics Letters **95**, 032904 (2009).

[25]   G. Wang *et al.*, Origin of the large electrostrain in $BiFeO_3$-$BaTiO_3$ based lead-free ceramics, Journal of Materials Chemistry A **7**, 21254 (2019).

[26]   Y. Kuroiwa, S. Kim, I. Fujii, S. Ueno, Y. Nakahira, C. Moriyoshi, Y. Sato, and S. Wada, Piezoelectricity in perovskite-type pseudo-cubic ferroelectrics by partial ordering of off-centered cations, Communications Materials **1**, 71 (2020).

[27]   I. Fujii *et al.*, Electric field induced lattice strain in pseudocubic $Bi(Mg_{1/2}Ti_{1/2})O_3$-modified $BaTiO_3$-$BiFeO_3$ piezoelectric ceramics, Applied Physics Letters **108**, 172903 (2016).

[28]   Z. Lu *et al.*, In situ poling X-ray diffraction studies of lead-free $BiFeO_3$–$SrTiO_3$ ceramics, Materials Today Physics **19**, 100426 (2021).

[29]   R. Dittmer, W. Jo, J. Rödel, S. Kalinin, and N. Balke, Nanoscale Insight Into Lead-Free BNT-BT-xKNN, Advanced Functional Materials **22**, 4208 (2012).

[30]   X. Liu, S. Xue, F. Li, J. Ma, J. Zhai, B. Shen, F. Wang, X. Zhao, and H. Yan, Giant electrostrain accompanying structural evolution in lead-free NBT-based piezoceramics, Journal of Materials Chemistry C **6**, 814 (2018).

[31]   M. Basham *et al.*, Data Analysis WorkbeNch (DAWN), Journal of Sychrotron Radiation **22**, 853 (2015).

[32]   J. Filik *et al.*, Processing two-dimensional X-ray diffraction and small-angle scattering data in DAWN 2, Journal of Applied Crystallography **50**, 959 (2017).

[33]   J. L. Jones, B. J. Iverson, and K. J. Bowman, Texture and Anisotropy of Polycrystalline Piezoelectrics, Journal of the American Ceramic Society **90**, 2297 (2007).

[34]   A. De Backer, K. H. W. van den Bos, W. Van den Broek, J. Sijbers, and S. Van Aert, StatSTEM: An efficient approach for accurate and precise model-based quantification of atomic resolution electron microscopy images, Ultramicroscopy **171**, 104 (2016).

[35]   S. Van Aert, A. De Backer, G. T. Martinez, A. J. den Dekker, D. Van Dyck, S. Bals, and G. Van Tendeloo, Advanced electron crystallography through model-based imaging, IUCrJ **3**, 71 (2016).

[36]   E. Aksel, J. S. Forrester, J. C. Nino, K. Page, D. P. Shoemaker, and J. L. Jones, Local atomic structure deviation from average structure of $Na_{0.5}Bi_{0.5}TiO_3$: Combined x-ray and neutron total scattering study, Physical Review B **87**, 104113 (2013).

[37]   B. Narayan, J. S. Malhotra, R. Pandey, K. Yaddanapudi, P. Nukala, B. Dkhil, A. Senyshyn, and R. Ranjan, Electrostrain in excess of 1% in polycrystalline piezoelectrics, Nature Materials **17**, 427 (2018).

[38]   R. D. Shannon and C. T. Prewitt, Effective ionic radii in oxides and fluorides, Acta Crystallographica Section B **B25**, 925 (1969).

[39]   H. Huang, G. Zhang, X. Ma, D. Liang, J. Wang, Y. Liu, Q. Wang, and L.-Q. Chen, Size effects of electrocaloric cooling in ferroelectric nanowires, Journal of the American Ceramic Society **101**, 1566 (2018).

[40]   R. Gao, J. Wang, J. Wang, and H. Huang, Investigation into electrocaloric effect of different types of ferroelectric materials by Landau-Devonshire theory, Acta Physica Sinica **69**, 217801 (2020).

[41]   K. Xu, X. Shi, S. Dong, J. Wang, and H. Huang, Antiferroelectric Phase Diagram Enhancing Energy-Storage Performance by Phase-Field Simulations, ACS Applied Materials & Interfaces **14**, 25770 (2022).

[42]   S. Xu, X. Shi, H. Pan, R. Gao, J. Wang, Y. Lin, and H. Huang, Strain Engineering of Energy Storage Performance in Relaxor Ferroelectric Thin Film Capacitors, Advanced Theory and Simulations **5**, 2100324 (2022).